Ultramicroscopy 266 (2024) 114034

Contents lists available at ScienceDirect

Ultramicroscopy

journal homepage: www.elsevier.com/locate/ultramic

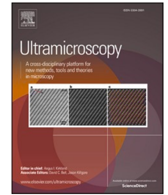

The impact of electric field strength on the accuracy of boron dopant quantification in silicon using atom probe tomography

Bavley Guerguis [a,*], Ramya Cuduvally [a,b], Richard J.H. Morris [c], Gabriel Arcuri [b], Brian Langelier [a,b], Nabil Bassim [a,b]

[a] Department of Materials Science and Engineering, McMaster University, Hamilton, ON L8S 4L7, Canada
[b] Canadian Centre for Electron Microscopy, McMaster University, Hamilton, ON L8S 4M1, Canada
[c] IMEC, Kapeldreef 75, 3001 Leuven, Belgium

ARTICLE INFO

Keywords:
Atom probe tomography
Semiconductor
Boron
Electric field
Dopant
Surface migration

ABSTRACT

This study investigates the impact of the surface electric field on the quantification accuracy of boron (B) implanted silicon (Si) using atom probe tomography (APT). The Si Charge-State Ratio (CSR(Si) = Si^{2+}/Si^{+}) was used as an indirect measure of the average apex electric field during analysis. For a range of electric fields, the accuracy of the total implanted dose and the depth profile shape determined by APT was evaluated against the National Institute of Standards and Technology Standard Reference Material 2137. The radial (non-)uniformity of the detected B was also examined. At a higher surface electric field (i.e., a greater CSR(Si)), the determined B dose converges on the certified dose. Additionally, the depth profile shape tends towards that derived by secondary ion mass spectrometry. This improvement coincides with a more uniform radial B distribution, evidenced by desorption maps. In contrast, for lower surface electric fields (i.e., a lower CSR(Si)), the B dose is significantly underestimated, and the depth profile is artificially stretched. The desorption maps also indicate a highly inhomogeneous B emission localized around the center of the detector, which is believed to be an artifact of B surface migration on the tip of the sample. For the purposes of routine investigations of semiconductor devices using APT, these results illustrate the potential origin of quantification artifacts and their severity at different operating conditions, thus providing pathways towards best practices for accurate and repeatable measurements.

1. Introduction

The ability to reliably characterize dopants within site-specific regions of a device is of significant interest to the semiconductor industry, as outlined in the International Roadmap for Devices and Systems (IRDS) [1]. Since the concentration and spatial distribution of impurities influence the electrical and optical properties of a device, assessing local defects in dopant architecture (e.g., in/out diffusion, clusters, and segregation) is essential for understanding the operational efficiency. For instance, the depth profile of implanted boron (B) in several matrices, such as silicon (Si), is known to be prone to broadening. This is characterised by a large shoulder in the concentration profile towards the substrate, which is a result of a diffusion-driven process during post-implantation annealing [2,3]. Effects such as diffusion, amongst others, can have detrimental consequences on the effective functionality of a device (e.g., threshold voltage variance [4] and electrical activation of dopants [5]) and restrict the ability to fabricate highly localized doped regions. As B is the most widely used *p*-type dopant in Si-based semiconductor devices, the ability to accurately quantify B content, down to several atomic parts per million, is crucial when evaluating deficiencies/enhancements in the performance, and/or assessing the manufacturing quality. However, this scope of investigation can be challenging due to the geometric complexity and continued miniaturization of individual components in micro-devices.

Atom probe tomography (APT) is a material characterization technique that has the potential to meet the demands of the IRDS given its unique ability for chemical mapping of three-dimensional features at the nanoscale [6]. However, the integrity of the collected data can often be reduced by measurement artifacts. To some extent, this has currently limited the widespread applicability of APT. In particular, preferential detection losses may cause compositional biases that impede rigorous quantification of certain elemental species (e.g., C [7–9] and B [7, 10–12]). Such losses can occur during an experiment (i.e., due to physical processes) or because of limitations in the data treatment

* Corresponding author.
E-mail address: guerguib@mcmaster.ca (B. Guerguis).

https://doi.org/10.1016/j.ultramic.2024.114034
Received 5 March 2024; Received in revised form 5 July 2024; Accepted 18 August 2024
Available online 21 August 2024
0304-3991/© 2025 The Authors. Published by Elsevier B.V. This is an open access article under the CC BY license (http://creativecommons.org/licenses/by/4.0/).

process. In general, for dopants in semiconductors, APT quantification accuracy is assessed by agreement with other techniques, primarily secondary ion mass spectrometry (SIMS).

The quantification accuracy for the B dopant in Si using APT has been reported with varied results; some studies show good accuracy (i.e., concentration profile agreement with SIMS) [13–16], while others report detection losses ranging from 10 to 50 % [7,10,12,17–19] as well as implant profile shape deviations compared to that which is expected [11,12,19–22]. Issues regarding the quantification accuracy may stem from complex field evaporation mechanics, believed to be a consequence of the significant differences in the field evaporation thresholds between the relatively high-field B impurities and the low-field Si matrix [18]. As such, B tends to be preferentially retained on the apex until the specimen reaches a sufficient surface enrichment [10,12,23], after which the evaporation of B is facilitated through local field enhancement by neighbouring atoms [12,24]. For an implanted Gaussian dopant profile, this predisposition for non-stoichiometric evaporation results in a comparatively elongated depth profile shape compared to a SIMS-acquired measurement.

Another artifact to consider is the degradation of the radial uniformity because of B atoms migrating across the specimen surface. In APT data, this typically manifests as an artificial enrichment of such solute atoms within the high-field regions (e.g., crystallographic poles and zone axes). Surface migration has been observed experimentally using field ion microscopy (FIM) [25,26] and investigated for various material systems including B-doped Si [12,23,27] and a number of solutes (e.g., N, C, P) in Fe and Ni [25,28], among others [29–31]. Some results suggest that it is a thermally-activated, field-driven process, such that a higher laser pulse energy and/or specimen base temperature increases the probability for migration. For instance, Tu et al. [23] showed that migration is enhanced by high laser pulse energies for B-doped Si. With an increase in laser power, elemental maps showed the B distribution to be less homogenous and localized at grain boundaries, an artifact that is attributed to migration and subsequent evaporation from these high-field regions. Conversely, Oberdorfer et al. [31] employed a combined finite element and molecular dynamics simulation, where specimen temperature was not considered, to model the surface migration tendency of Cu in an Al matrix. Their simulation results, validated by experimental observations, suggest athermal relaxation as a primary mechanism. In short, the Cu atoms migrate to the crystallographic poles through a series of relaxation events to energetically preferred neighbouring sites vacated by preferentially evaporated Al atoms. Thus, migration can be considered as a complex phenomenon, with contributions from several physical processes, as well as a likely dependence on APT experimental conditions and the material system analyzed. In the case of B-doped Si, it is important to consider the possibility of B atoms migrating prior to their emission. This will result in their recorded position not being representative of their original location at the tip apex and may subsequently result in artificial concentration variations [25].

Extensive migration may also increase the natural tendency of B to co-evaporate in burst, or so-called multiple-hit (multi-hit), events which can lead to its undercounting. This is because, without sufficient separation in space and time, the three-anode delay-line detector systems used in modern commercial atom probes cannot resolve co-evaporated ions. This is due to an associated dead-zone and dead-time ($\sim$3 ns for the CAMECA LEAP 5000 XS and XR [32]) following each detection event; also known as detector pile-up/saturation. Significant B detection losses have been reported as a consequence of multi-hit events specifically involving same isotope same charge-state (SISCS) ions, as demonstrated by Meisenkothen et al. [10]. This is because these types of co-evaporated ions will experience no, or insufficient, separation in space and time. In their study [10], B signal losses are measured to be 20 % for a straight flight-path instrument (LEAP 4000X-Si) and 36 % for a reflectron-fitted instrument (LEAP 4000X-HR). The magnitude of error has been reported to increase with higher B concentrations owing to an increased probability of SISCS co-evaporation [17].

An additional level of complexity that can arise, and not previously explored for this material system, is that the composition determined by APT may be affected by the experimental conditions employed [33–36]. For B, a higher electric field has been shown to improve the B depth profile agreement with SIMS, as demonstrated in a study of a B-doped SiGe structure [11]. Melkonyan [12] explored different experimental conditions for B-doped Si systems, likewise reporting an improvement in the concentration values and profile shape agreement with SIMS for higher electric fields. Although these results collectively demonstrate the potential of achieving accurate B quantification using APT through the optimization of experimental conditions, the severity of observed detection losses at various field conditions has yet to be thoroughly explored. Additionally, since at any given electric field condition there are multiple physical mechanisms that could play a role in compositional biases, the interplay between these various effects needs to be investigated in detail. Thus, a systematic study is critical for understanding the origin of these inaccuracies, reducing quantification uncertainty, establishing best practices, and defining optimal experimental parameters for the routine analysis of B-doped Si devices.

A study of this nature demands the use of a well-characterized sample for which the dopant dose and its depth profile are accurately known. This motivated the choice of using the National Institute of Standards and Technology (NIST) Standard Reference Material (SRM) 2137 [37]. Building on the preceding work [10–12] and considering the aforementioned points, the present research aims to provide a holistic investigation into the impact of the electric field strength on B quantification accuracy. The data treatment process is discussed in detail to facilitate measurement repeatability and minimize user-dependent biases. Si quantification accuracy is also evaluated using a standard CAMECA pre-sharpened microtip (PSM) coupon [38], since any undercounting of the matrix species will lead to an erroneous dopant concentration measurement.

2. Materials and methods

2.1. Materials and sample preparation

The NIST SRM2137 [37] is ^{10}B-implanted Si, with Si in the doped region amorphized prior to ion implantation to yield a shoulder-free B concentration profile. It has a certified dose of 1.018×10^{15} atoms/cm^2, as measured by neutron depth profiling (NDP). The B depth profile shape was measured by SIMS, with the depth scale determined using the crater depth measured by stylus profilometry. This shows an implanted region spanning approximately 400 nm in depth, with a peak concentration of 8.37×10^{19} atoms/cm^3 188 nm beneath the surface.

The wafer was cleaned using sonicated acetone and isopropyl alcohol baths (5 minutes each), rinsed with deionized water, and dried. The surface was sputter coated with a $\sim$250 nm Cr layer using a Quorum 300T D Plus. The Cr-cap was added to protect the near-surface region of interest (ROI) from beam damage during APT sample preparation [39]. A small part of the Cr capping layer ($<$ 25 nm) was retained on each of the final specimens to avoid milling damage in the ROI, but also aid in the precise identification of the concentration profile starting point during data analysis. Specimen preparation was performed in a Thermo Scientific Helios 5 UC DualBeam, equipped with a Ga^+ source, following the standard focused ion beam-scanning electron microscope (FIB-SEM) lift-out procedure for APT samples [40] (Fig. 1). This was finished with a 2 kV final cleaning step to minimize the ion beam damage in the prepared specimens.

2.2. APT analysis

Since it is not possible to access the specimen end-radius during an APT experiment, the charge-state ratio (CSR) is typically used as an indirect measure of the average electric field at the apex. Kingham showed that the fraction of multiply-charged ions (i.e., X^{i+} for $i = 2$, 3,

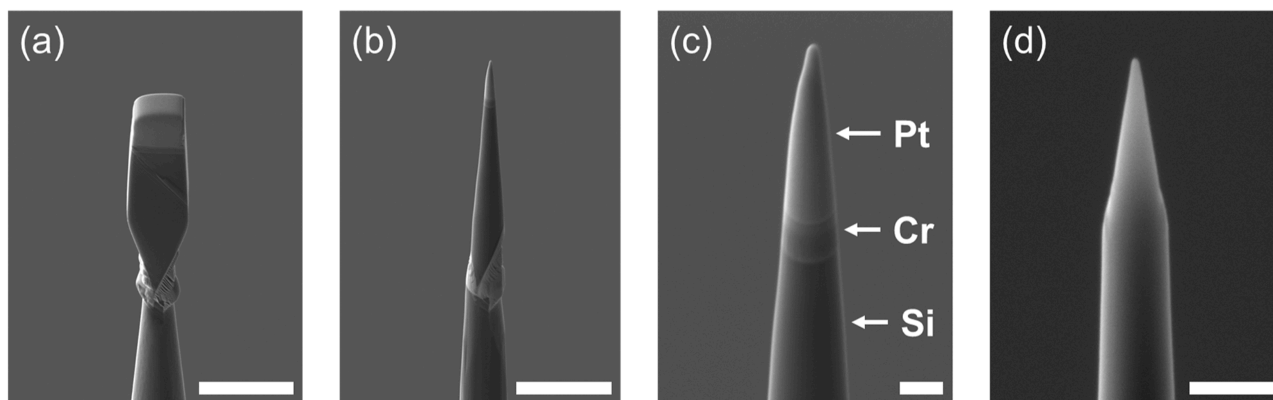

Fig. 1. SEM images throughout the sample preparation procedure, captured at a 52° stage tilt. (a) A wedge attached to a Si micro-tip post by FIB Pt deposition after lamella lift-out and propagation. (b) A wedge following a series of annular milling processes for specimen shaping and thinning. (c) Pt and Cr layers on a specimen prior to the final annular milling steps and 2 kV cleaning. (d) A prepared sample ready for APT analysis. The scale bars in (a) and (b) are 5 μm, and in (c) and (d) are 500 nm. All images are tilt-corrected.

…) detected during an experiment increases with increasing electric field strength [41]. Post-ionization theory defines a pathway for relating the charge-state abundances to the average electric field strength at the apex during field evaporation. Throughout this study, the Si charge-state ratio (CSR(Si)), which is the ratio of the number of counts in the 14 and 28 Da peaks (Si^{2+}/Si^{+}) within a portion of the ion sequence, is used to evaluate the average electric field strength during an APT experiment. For laser-assisted APT at a constant detection rate, the applied electric field strength (and therefore the measured CSR(Si)) is inversely related to the laser pulse energy received by the specimen. In general, a lower laser pulse energy (i.e., a lower apex temperature) must be compensated by a higher DC bias to maintain a constant detection rate, resulting in a higher electric field at the apex. Conversely, a higher laser pulse energy (i.e., a higher apex temperature) allows achieving the target detection rate with a lower DC bias, resulting in a lower electric field at the apex.

APT data was acquired in laser-pulse mode on a CAMECA LEAP 5000 XS, which has a straight flight-path. It is equipped with a 355 nm wavelength ultraviolet (UV) laser and has a detection efficiency of approximately 80 %. First, the laser pulse energy and detection rate were set to 50 pJ and 0.0025 ions/pulse (0.25 %), respectively. This was maintained until complete evaporation of the Cr-cap was achieved, thereby minimizing any induced stress on the specimens and avoiding premature fracture at the Cr-Si interface. Following the field evaporation of the Cr-cap, the detection rate was increased to 0.005 ions/pulse (0.5 %) and auto pulse energy control (APEC) enabled. With APEC, the laser pulse energy is automatically adjusted to achieve, then maintain, a specified target CSR based on the ratio of two user-selected ranges in the mass spectrum over a portion of the ion sequence (e.g., $Si^{2+}/Si^{+} = 10$). This mode of operation was used to minimize field variations throughout the analysis and create relatively constant evaporation conditions. With a constant laser pulse energy, as typically used in APT analysis, a natural increase of the end-radius due to a non-zero shank angle, in addition to variations in FIB-induced damage down the length of the specimen, may result in undesirably large variations in the CSR from a starting value [42,43]. This would complicate any subsequent comparative analysis between samples. Moreover, for specimens analyzed at the highest-field conditions, a large increase in CSR increases the risk of premature fracture.

Six samples were analyzed at CSR(Si) targets of 0.25, 0.5, 10, 30, 60, and 80. In each case, the base temperature was set to 50 K, and auto pulse rate control (APRC) was enabled at a mass-to-charge-state upper limit of 250 Da. APRC expedites data acquisition time by automatically increasing the laser pulse rate during an experiment to compensate for an increasing specimen voltage and a decreasing time-of-flight. Although this means that the laser pulse rate does vary during each analysis, it is not expected that this has a significant impact on the results for a number of reasons. First, the frequency range for samples 2–6, as reported in Table 1, is relatively narrow and a significant portion of all experiments were conducted at 555 kHz. Second, there is minimal variance in the average laser pulse frequency across all six samples. Finally, the laser pulse frequency has been previously shown to have a minimal impact on preferential evaporation for minerals [44], alloys [45], and semiconductors [46]. For each experiment, CSR(Si) history plots are shown in Fig. 2(a) (excluding the Cr-cap).

All but sample 2 experience a maximum deviation in CSR(Si) over the analysis depth of <20 % of the target value. For sample 2, there is an initial rapid increase in the CSR(Si) to 0.7 (i.e., 140 % of the target value), followed by an abrupt drop to 0.5 at approximately 15 million ions. As well, for sample 3, the CSR(Si) does not stabilize until about 20 million ions. While these are not negligible variations, the differences in the average magnitude of CSR(Si) experienced by each sample does allow a comparative analysis for the purposes of this investigation, as can be seen in Fig. 2(b). However, given that the CSR(Si) remains relatively constant for samples 1 and 6, and these samples were measured at the two most extreme conditions (i.e., lowest and highest electric fields), all comparative analysis will be performed using these two datasets. The results from the other four samples are included to illustrate the electric field dependence between the two extremes.

2.3. Data reconstruction

Data reconstruction was performed using the CAMECA AP Suite 6 software [47]. For each specimen, the radius evolution was based on a tip-profile determined from an SEM image acquired prior to APT analysis. While some degree of measurement error may be present in the radius evolution using this method, this was assessed to be the most accurate technique over voltage-based or fixed shank-based radius evolutions. The image compression factor (ICF) was constrained using the measured evaporation depth by correlating pre- and post-analysis images with the aid of local topographic features (Fig. 3(a)). The non-tangential continuity ratio [48] was also measured from the post-analysis image for each specimen (Fig. 3(b)). This ratio provides a more accurate reconstruction in the depth dimension, which is critical for dose quantification and profile shape integrity [49]. The ICF for each sample is given as follows: sample 1 – 1.95, sample 2 – 1.84, sample 3 – 1.77, sample 4 – 1.96, sample 5 – 1.66, and sample 6 – 1.73.

Table 1
Summary of relevant acquisition conditions.

Sample	Target CSR(Si)	Average CSR(Si)	Average Laser Pulse Energy	Laser Pulse Frequency		Average Background	Chamber Pressure
				Range	Average		
	Si^{2+}/Si^{+}	Si^{2+}/Si^{+}	*pJ*	*kHz*	*kHz*	*ppm/ns*	$\times 10^{-9}$ *Pa*
1	0.25	0.24 ± 0.01	41.1 ± 1.7	294 to 555	508 ± 45	5.2	7.77
2	0.5	0.52 ± 0.04	36.5 ± 1.6	384 to 555	497 ± 44	5.3	7.49
3	10	9.55 ± 0.55	24.6 ± 1.2	416 to 555	533 ± 33	8.2	11.89
4	30	28.88 ± 1.70	16.9 ± 0.8	416 to 555	530 ± 35	10.3	9.62
5	60	61.29 ± 2.34	10.4 ± 0.6	416 to 555	534 ± 32	24.8	7.38
6	80	80.42 ± 1.65	8.8 ± 0.5	454 to 555	533 ± 32	26.7	7.49

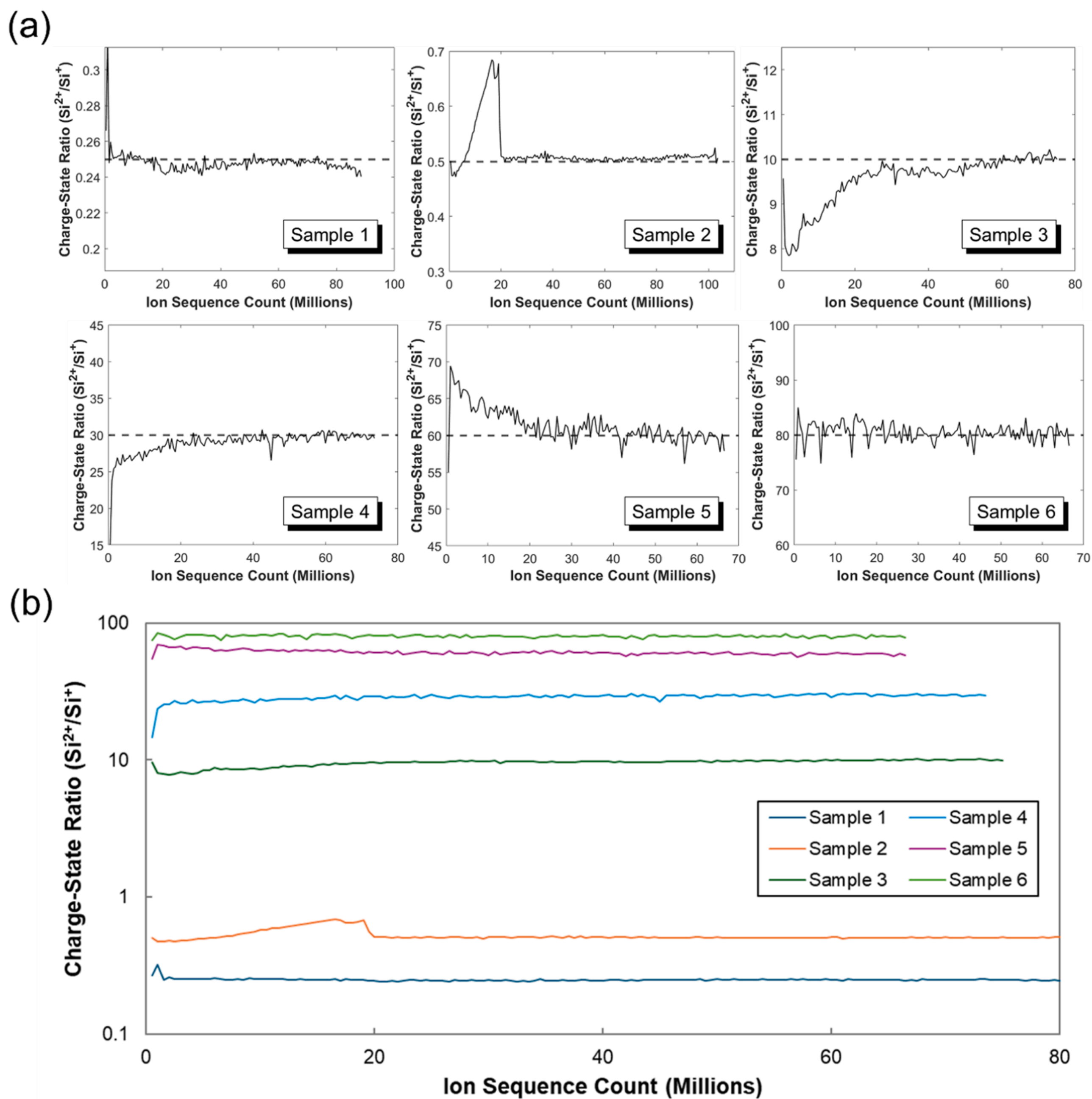

Fig. 2. (a) CSR(Si) evolution plots as a function of ion sequence count, excluding the Cr-cap. The black dashed lines represent the specified CSR(Si) target value for each sample. (b) Composite CSR(Si) evolution plot with all samples included for the first ~80 million ions collected.

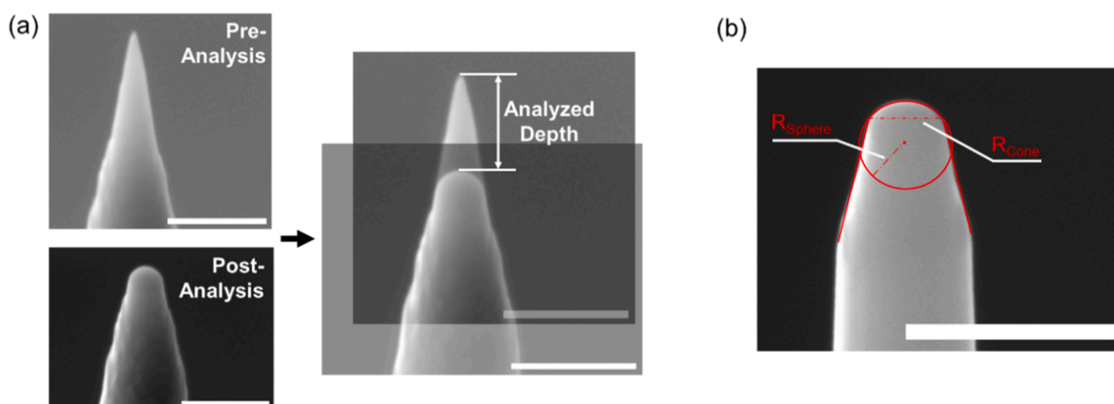

Fig. 3. (a) An example of the reconstruction-constraining procedure, whereby the evaporation depth is measured by correlating pre- and post-analysis SEM images. (b) An example of non-tangential continuity, measured by the ratio R_{Sphere}/R_{Cone} (the radii of the sphere and cone, respectively). All scale bars are 500 nm.

3. Results and discussion

3.1. B quantification accuracy

Fig. 4(a) presents a representative mass spectrum of the NIST SRM2137, with all the major ion peaks labelled appropriately. For all the peaks identified, the range bounds were guided by the local background levels (i.e., the start and end bounds were chosen at the points where the peak crosses the estimated background level [12]). Additional Si molecular ions, namely Si_2^+, SiO^+, and $SiOH^+$, were identified in the mass spectra of samples 1 and 2 (not shown), which were analyzed at the two highest average laser pulse energies.

The unlabelled peaks between 35 and 48 Da were present in each mass spectrum collected but could not be unequivocally identified. While these are likely complex molecular ions containing Si (e.g., SiN_3^{2+} or Si_2N^+ at 35/35.5/36 Da, SiO^+ and/or $SiOH^+$ at 44/45/46 Da, and SiF^+ at 47 Da), their lack of inclusion is not expected to significantly impact the presented data as all mass spectra were treated consistently (i.e., peaks identified and ranged). As well, the magnitude of the largest unidentified peak (35 Da) is just 0.1 % of the dominant Si^{2+} peak. Still, a sensitivity analysis was conducted by ranging these peaks as Si and assessing the impact on B dose measurements. The effect was found to be most pronounced for sample 6, but reducing the dose by just 1.55 %; a difference within the error bar ranges presented below.

With <1 % of the total dose being ^{11}B [37], the B in SRM2137 can be considered monoisotopic. Thus, the 11 Da and 12 Da peaks are assumed to be $^{10}BH^+$ and $^{10}BH_2^+$, respectively. All background corrections were performed using a local range-assisted power law model within AP Suite 6. Fig. 4(b) shows an example of a reconstructed dataset.

One-dimensional B concentration profiles were calculated along the longitudinal axis of each sample, with the full reconstructed volume (Fig. 5). This was done using atomic percentages of B and Si for a 2 nm bin width, starting at the Si-Cr interface. Then, this was converted to atoms/cm^3 using the theoretical Si atomic density of 4.99×10^{22} atoms/cm^3 [50]. It is important to note that the Si atomic density may be slightly higher for the SRM2137 as a result of the ^{28}Si implantation. However, Stopping and Range of Ions in Matter (SRIM) [51] simulations found a peak implanted ^{28}Si concentration of just 0.2 at.% (i.e., an atomic density of approximately 5.2×10^{22} atoms/cm^3) and, therefore, this is not expected to have a significant influence on the results presented.

The statistical significance of a B signal was assessed using the following criterion at each interval,

$$n_B - \sqrt{n_B(1-Q)} > n_{BL} - \sqrt{n_{BL}(1-Q)} \tag{1}$$

where n_B is the number of B counts, n_{BL} is the number of background counts, and Q is the detector efficiency (~80 % for CAMECA LEAP 5000 XS) [52]. The background counts are based on equal-width ranging of adjacent regions to the $^{10}B^+$ peak.

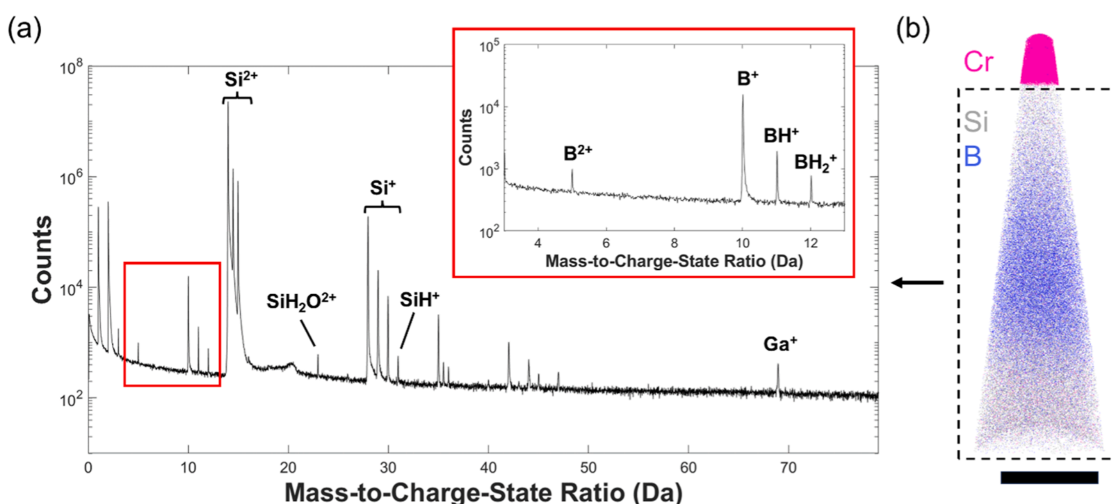

Fig. 4. (a) A representative mass spectrum (excluding the Cr-cap) acquired from the NIST SRM2137 (sample 6, CSR(Si) = 80). The top-right inset shows a zoomed-in section of the mass spectrum with B^{i+} and BH_i^+ peaks labelled accordingly. (b) An example of an APT dataset reconstruction with the Cr-cap at the top and a B gradient in a Si matrix below. The scale bar in (b) is 100 nm.

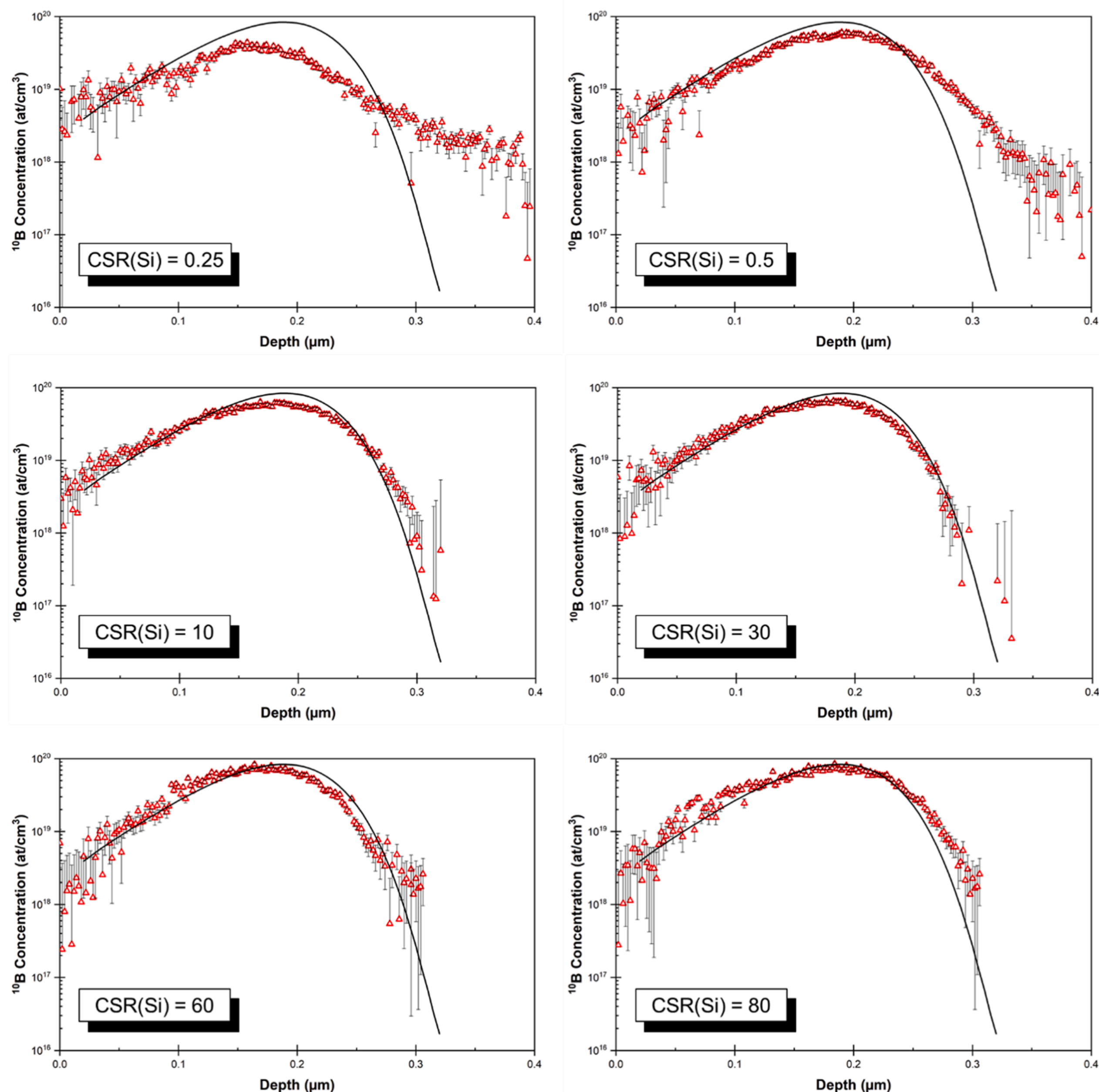

Fig. 5. Bulk volume B concentration profiles measured at each field condition. The black line is the SIMS-acquired profile shape [37]. Note that the SIMS shape is not certified by NIST.

The APT B depth profile integrity was evaluated based on its agreement with the SIMS-measurement. While the SIMS profile is not certified by NIST, it is reasonable to expect that the reported depth profile is representative [53]. As previously described [11,12,19–21] and presented here, samples that are analyzed at low-field (i.e., high laser pulse energy) have a depth elongated B concentration profile. This manifests itself into a higher-than-expected B concentration within the tails of these profiles. These two characteristics are likely due to B retention on the surface from insufficient evaporation conditions [12, 23]. Increasing the apex electric field strength improves the profile shape by bringing it in agreement with that measured by SIMS, although negligible improvements are observed between the CSR(Si) range of 30 and 80. The small differences between the APT profile shapes at the highest electric field conditions compared to SIMS is believed to be a result of imprecisions in the reconstruction (e.g., use of a constant ICF [54]) and misalignment between the implantation and analysis axes.

The B implant dose was determined by integrating each of the bulk volume concentration profiles (Fig. 5) (i.e., calculating the area under the curve). Fig. 6 shows the B dose measurements as a function of CSR (Si) and the estimated electric field from Kingham's post-ionization theory [41]. Other reported SRM2137 dose measurements by APT [10,12] are included in this plot. The B quantification accuracy relative to the NIST certified NDP dose value improves substantially with increasing electric field. At a CSR(Si) of 0.25, approximately 53.6 % of the expected dose was measured. This significantly increases to 80.9 % at a CSR(Si) of 0.5. Interestingly, by raising the CSR(Si) from 10 to 30, it remains invariant within the analysis error. It is at a CSR(Si) of 60 where the B dose again improves, now increasing to approximately 94.0 % of the certified dose. Finally, at a CSR(Si) of 80, the measured dose exceeds the NDP value (i.e., found to be 104.7 %). This overestimation will be revisited in Section 3.3.

As some degree of uncertainty will be present in the reconstructions,

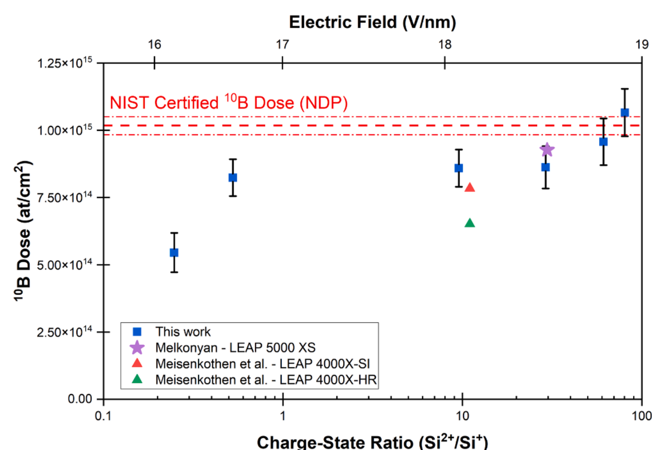

Fig. 6. Measured ^{10}B dose as a function of CSR(Si), with an estimate of the electric field shown on the top axis. The error presented for each dose is the sum of the B standard error due to counting statistics in each of the 2 nm concentration profile bins. Other literature [10,12] results are included in this plot. The reported uncertainty in the certified dose [37] is represented above by the red dot-dash horizontal lines.

a sensitivity analysis was performed for samples 1 and 6 to investigate the impact of ICF variance on the measured B dose. The tip profile definitions and the non-tangential continuity ratios were held constant, while the ICF was varied by increments of ±5 %, and the B dose for each ICF condition was then determined. In all cases but for −15 % and −10 % of the ICF for sample 6, the B dose was found to be within the reported error bars in Fig. 6. This demonstrates that, while there may be some level of uncertainty that is present in the reconstructed volume parameter, it is still reasonable to expect that the presented results are sufficiently accurate and enable a comparative analysis.

Comparing the results presented in this study with those reported previously highlights an important issue which currently impedes routine analysis by APT. That is measurement reproducibility arising from instrument and/or user-induced biases. For instance, despite analysis at a CSR(Si) of between 10 to 12 [55], Meisenkothen et al. report a B dose value using the LEAP 4000X-HR, a reflectron-fitted instrument, that is more comparable to the values reported here at low-field conditions and for a straight flight-path tool. While the other two literature values which were also measured using straight flight-path instruments show a small improvement, they still offer unsatisfactory agreement. This underlines the significance of considering inconsistencies in data treatment methodologies as a contributing source of measurement discrepancies and the need for developing standardized methods for constraining these processes (e.g., mass spectrum ranging [56] and ICF calibration [57]). There is also a pressing requirement for understanding how instrument design/configuration influences the field evaporation physics and the associated impact on compositional biases.

3.2. *Mechanism of quantification improvement*

To understand the mechanism behind the improvement in B quantification accuracy, it is critical to consider multi-hit events, which form the majority for B detection. In fact, for the sample analyzed at the lowest electric field, approximately 69 % of the B detected occurs as a multi-hit event. In contrast, only 2 % of the Si was detected as a multi-hit event for the same sample. Fig. 7(a) shows the impact of CSR(Si) on B detection events by hit type. With an increasing CSR(Si), the fraction of B detected as a single-hit event increases, while the fraction of B detected in a double-hit event decreases. It is unclear why this trend reverses when going from a CSR(Si) of 60 to 80. Further investigations at even higher fields may help clarify this behaviour. However, increasing

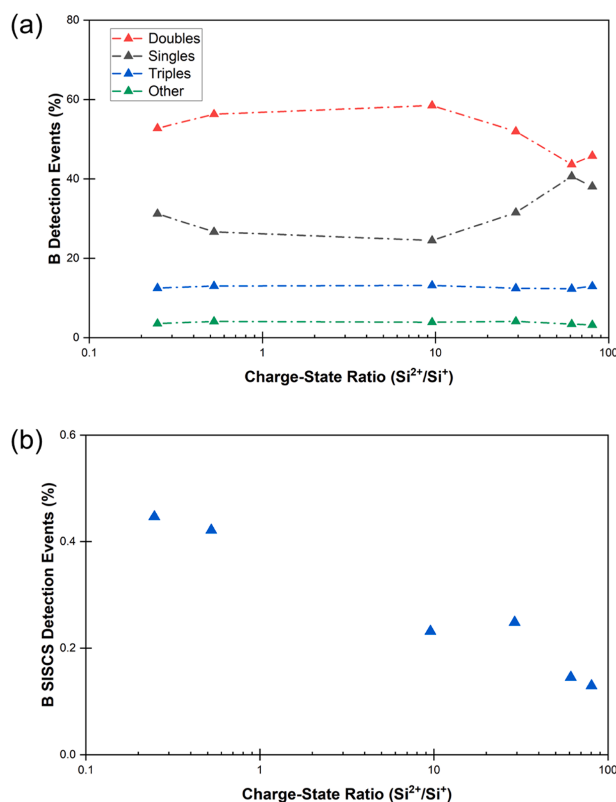

Fig. 7. (a) Impact of CSR(Si) on the fraction of B detected in single-hit, double-hit, triple-hit, and higher-order detection events. (b) Fraction of B SISCS detection events as a function of CSR(Si).

the CSR(Si) substantially (i.e., greater than 100) will result in a higher likelihood of specimen fracture due to the induced stress at higher electric fields, thereby complicating such an experiment and subsequent data analysis.

The primary source of the B underestimation is considered to be SISCS co-evaporation events [10,12,18]. Therefore, an improvement in B quantification accuracy is expected to correspond with a reduction in this type of detection (as a fraction of the total B detection). A thorough analysis of SISCS B detection is not possible since such higher order multi-hit events are often incorrectly recorded as being lower-order or single-hit events [18]. Nevertheless, Fig. 7(b) shows the fraction of B detected as SISCS double-hit events as a function of the CSR(Si), which decreases monotonically with increasing electric field. Fig. 7(b) qualitatively supports the field-dependent trend reported in Fig. 6, which is that a more accurate B dose measurement corresponds with a lower fraction of SISCS B double-hit events. However, it is essential to emphasise that this a purely qualitative assessment and further investigations are required to better understand this trend. As in [10], a nominally pure B sample could be used to investigate B multi-hit events with the aid of natural isotopic abundances, but extending the investigation over a range of electric fields (as done here). This would provide a pathway for understanding B evaporation tendencies at different operating conditions. For a B-doped Si sample, Si complicates this type of analysis since it would likely be involved in B multi-hit events. Thus, it would be essential to consider higher-order detection events with various combinations of B and Si isotopes and/or charge-states, an arduous task.

It is proposed that the reduction in B multi-hit events with increasing electric field (Fig. 7(a)) is a consequence of reduced B mobility at the apex. Under non-ideal analysis conditions (i.e., a high laser pulse energy and/or a high base temperature), these atoms migrate and coalesce. They then co-evaporate in bursts which increases the probability of

SISCS evaporation, and subsequent detection loss. This is supported by Fig. 8, which presents the normalized detector density maps of Si, B, Si^{2+}, and Si^{2+} multi-hit events. The last two columns are meant to illustrate local regions on the detector (i.e., specimen surface) with a lower/higher electric field. Column 1 (i.e., the detector density maps of Si) is included as a reference; these maps approximately resemble the distribution of all hits acquired for these samples during analysis (excluding the Cr-cap).

For the sample analyzed at the lowest-field (CSR(Si) = 0.25, ~41 pJ), the Si^{2+} distribution (column 3) and the Si^{2+} multi-hit distribution (column 4) both show an increasing gradient across the detector, which points away from the laser-tip impact position towards the shadow-side. This artifact results from an asymmetrical tip shape evolution induced by the one-sided laser illumination of the specimen apex [58]. With a higher CSR(Si) and lower laser pulse energy (e.g., CSR(Si) = 80 at ~9 pJ), the Si^{2+} and the Si^{2+} multi-hit distributions become more uniform over the detector, indicating that the electric field is more homogeneous across the specimen surface. This, in turn, would suggest a more symmetrical tip shape, which is expected due to the lower laser pulse energy applied.

The most interesting aspect of Fig. 8 is the radial distribution of B events (column 2). A low-field (CSR(Si) = 0.25) produces a highly localized B detection map, centered on the detector and completely uncorrelated with the corresponding field distribution (columns 3 and 4). This is in stark contrast with the Si density maps (column 1), which approximately reflect the apex (a)symmetry in accordance with columns 3 and 4. As the CSR(Si) is increased, the B map becomes progressively more homogeneous, with the B starting to fill a greater fraction of the detector and producing a relatively uniform map at a CSR(Si) of 80.

Considering the uneven detection pattern of B at low-field, extensive migration, trajectory aberrations, or other artifacts would be required to explain such a limited detection area since the SRM2137 is uniformly doped in the radial dimension. Assuming the localized detection area, as observed for the CSR(Si)s of 0.25 and 0.5 in Fig. 8, is an artifact caused by migration before evaporation and detection, it is inconsistent with the expected migration tendency. The doped-region in SRM2137 is considered to be amorphous. Hence, crystallographic poles are not observed in the density maps (column 1 in Fig. 8). With a lack of crystallography, the field distribution is expected to be dependent on local atomic variations on the specimen surface; the overall tip shape; and the laser-tip interaction. Therefore, the expectation would be for the B to migrate towards (and be preferentially detected from) the shadow-side, where the field is highest.

To understand the detection tendency of B as a function of analysis depth, Fig. 9 shows the normalized detector density maps of Si, B, Si^{+}, and Si^{2+} for sample 1 (lowest-field analysis) and sample 6 (highest-field analysis) taken at 20 million ion increments, over the first 60 million ions collected. The density maps of sample 6 follow the expected behaviour, with the B detection and the field distribution remaining uniform across the surface at all stages of analysis. Each of the Si^{+} density maps show a high concentration on the laser-side, as expected from the one-side laser illumination of the sample.

However, for the first 20 million ions of sample 1, the B detection pattern appears to increase from the edge to the detector center. The Si^{+} and Si^{2+} maps for this increment indicate that the field is highest on the shadow-side, given that the doubly-charged Si species is concentrated in that region. The subsequent depth increments are notable for two reasons. First, the Si^{+} maps show a depleted region that has an inverse correspondence to the B density map. It is believed that this depletion is caused by the migration and retention of B at the center of the needle.

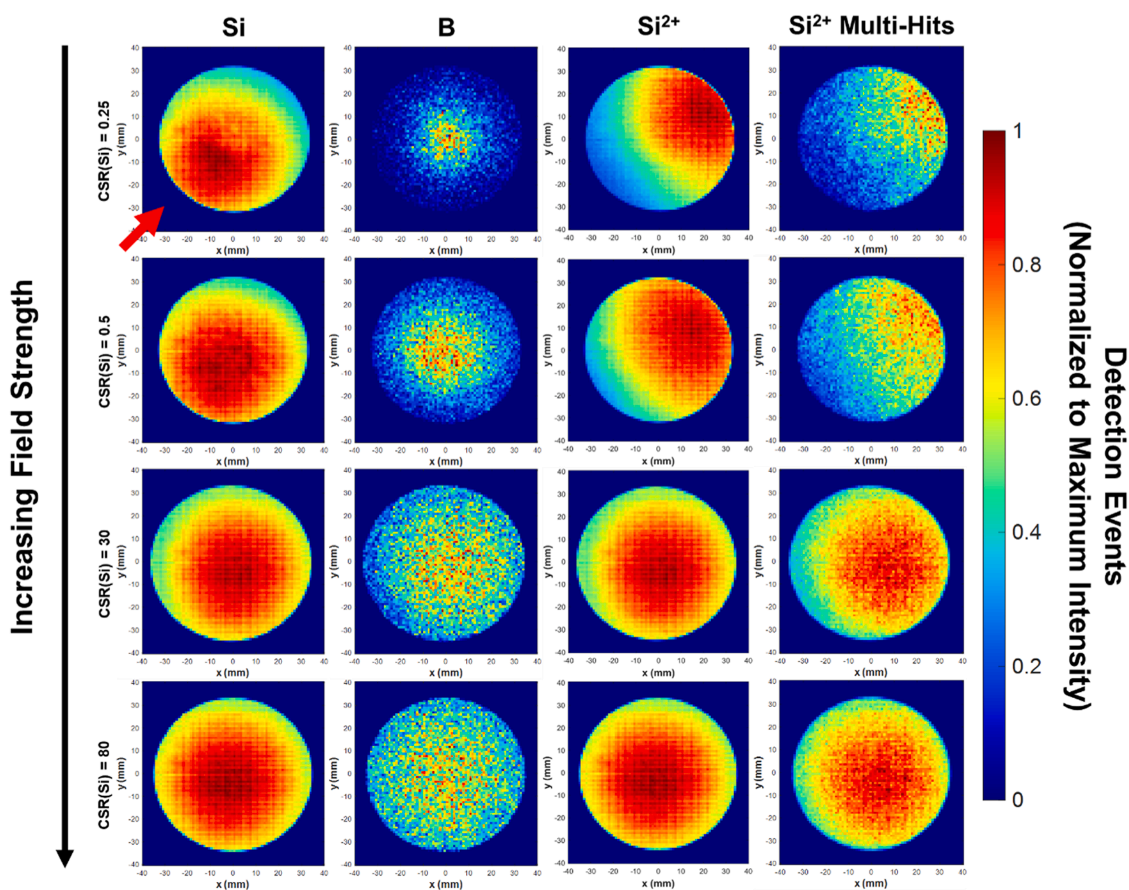

Fig. 8. Normalized detector density maps of Si, B, Si^{2+}, and Si^{2+} multi-hit detection events. Columns 3 and 4 are meant to illustrate local regions on the specimen surface that experience a higher electric field. The laser direction is indicated by the red arrow.

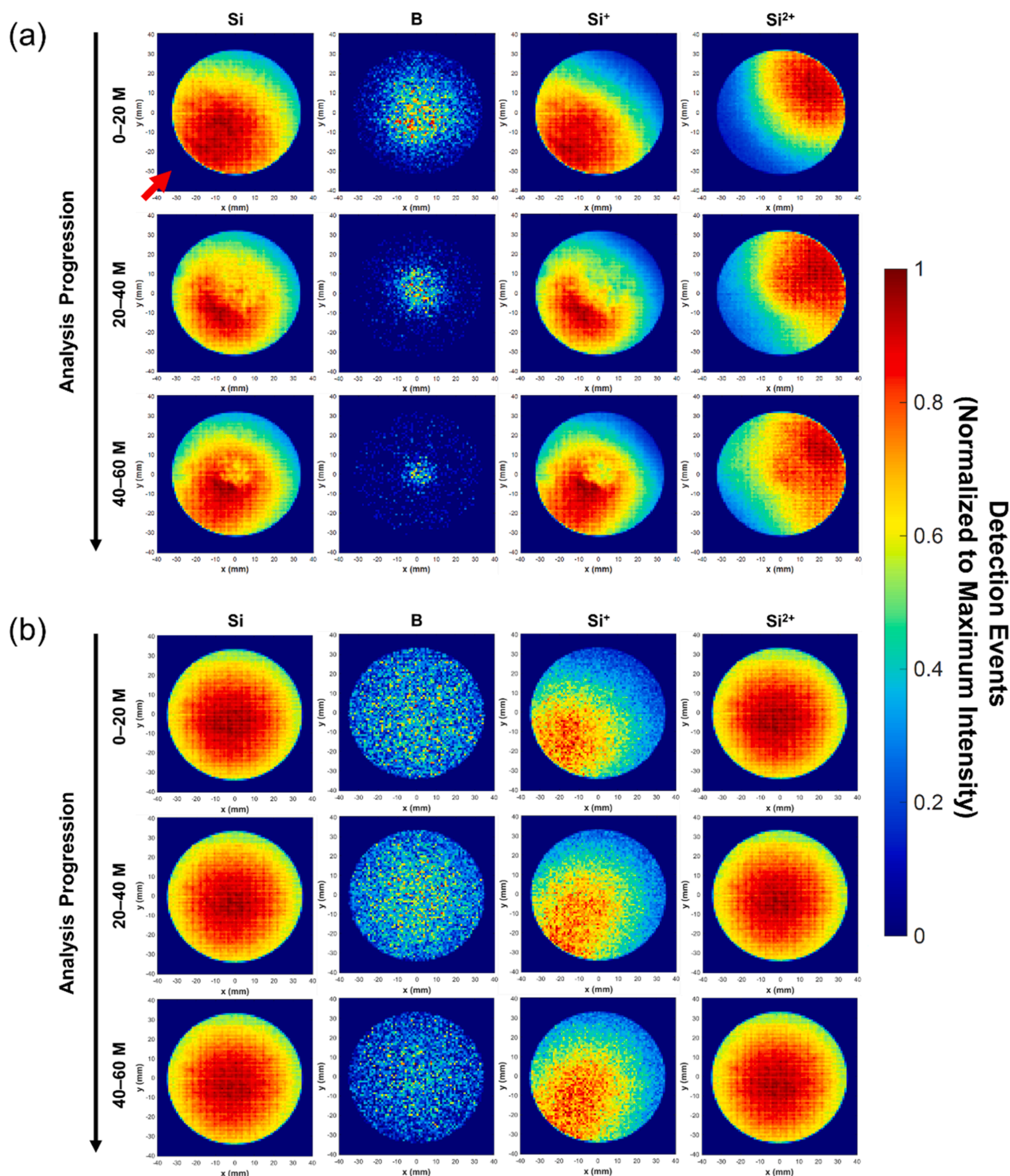

Fig. 9. Normalized detector density maps of Si, B, Si^{+} and Si^{2+} for (a) sample 1 (lowest-field analysis) and (b) sample 6 (highest-field analysis) at 20 million ion increments, for the first 60 million ions collected of each (excluding the Cr-cap). The laser direction is indicated by the red arrow.

Since B has a significantly higher evaporation threshold than Si, the evaporation of B within the center may only proceed when the local field is high enough. This would further suggest that this region has a locally high radius of curvature and consequently a higher local electric field, which increases the likelihood for post-ionization of Si^{+}, thereby facilitating its evaporation as a doubly-charged species.

Second, the B density maps show that the detection becomes more localized as the analysis progresses, despite the field distribution, as estimated by the Si^{2+} density maps, remaining generally constant. Surface migration of solutes has been previously described as a thermally-assisted, field-driven mechanism. Preferentially retained, high-field species migrate to high electric field regions, such as crystallographic poles and zone axes [25]. An alternative mechanism was proposed by Oberdorfer et al. [31] involving a directional walk of the solute atoms to the crystallographic poles through a series of relaxation events to energetically favourable sites. These are sites that are vacated by the evaporated matrix atoms. Since matrix atoms at kink sites of a terrace have the highest likelihood of evaporation [59], a receding terrace ledge guides a solute atom towards the most energetically favourable, high-neighbour-count site (i.e., a crystallographic pole). Thus, instead of an attraction to the high electric field regions, migration to crystallographic poles may be a result of the evaporation sequence which follows the crystallography of the sample under analysis. APT has been previously used to investigate amorphous materials (e.g., bulk metallic glasses [60,61]), with a non-uniform evaporation sequence reported [60]. As the SRM2137 lacks crystallography (i.e., long-range order) and therefore crystallographic poles, ordered evaporation of the Si and the subsequent directional walk of the B to the high electric field regions may not be expected. In other words, assuming athermal relaxation is the dominant mechanism of migration, there may not be any driving

force or physical process for which B should move towards the high electric field, shadow-side region. Still, it is not clear why B is being detected from the center of the needle and becomes more localized as the analysis progresses. Field evaporation simulations of an amorphous material would help elucidate any patterns or tendencies from the Si evaporation behaviour that could be driving B towards the center. Such simulations are outside the scope of this investigation, but future work is planned on investigating this in more detail.

Alternatively, it is possible that this anomaly is a result of a non-hemispherical tip shape, combined with field-of-view (FOV) aberrations. The limited absorption depth of the UV laser illumination by Si is known to result in severe asymmetry of the FOV region [58]. This has been demonstrated by Ling et al. [62] through evaporation simulations and corresponding hit maps. In short, an experiment begins by the laser-side of the sample eroding. This results in the laser-side radius increasing, reducing the probability of field evaporation for that side. To compensate, and for the analysis to proceed, atoms on the shadow-side experience a higher electric field and probability of evaporation. A steady-state apex shape is finally reached with a locally lower radius of curvature on the shadow-side and a higher radius of curvature on the laser-side. This causes the apex axis and the FOV to shift towards the shadow-side during an experiment. Since the field distribution maps do not consider the specimen outside of the FOV, the detector maps shown in Figs. 8 and 9 only describe local differences in the field distribution. Therefore, it is possible that B is migrating to the high electric field region, but this behaviour is being confounded by irregularities/aberrations in the FOV. Once again, future work is planned on understanding the tip shape impact on reconstruction artifacts and field evaporation tendencies.

3.3. Field strength impact on Si quantification

An additional consideration for this investigation was the impact of the electric field on the Si quantification accuracy. It is possible that a substantial loss of Si is artificially increasing the determined B dose, especially in the case of the overestimation observed in sample 6 (analyzed at the highest field). This can be assessed by comparing the apparent isotope fractions to the naturally occurring amounts ($X_{28_{Si}} = 92.23$ %, $X_{29_{Si}} = 4.67$ %, and $X_{30_{Si}} = 3.10$ % [63]). Any deviation from these values could be correlated with some degree of Si detection loss, for example, through multi-hits involving SISCS Si ions. Analysis of the apparent isotope abundances for the SRM2137 is complicated by the surface amorphization method prior to ion implantation, whereby the wafer is triply implanted with ^{28}Si ions at a dose of 2×10^{15} atoms/cm^2 using three impact energies (360 keV, 140 keV, and 50 keV [37]). In other words, the abundances are biased prior to APT analysis and the sample is not expected to have the natural isotope fractions within the ROI. Instead, a CAMECA PSM coupon [38] was chosen for the Si quantification analysis, which is done by assessing deviations in the natural abundances at various electric field conditions. This coupon contains a standardized array of (100)-oriented single crystal antimony (Sb) doped Si tips, typically used for detector and laser alignments.

Si quantification analysis using the PSM was conducted at a constant detection and laser pulse rate of 0.005 ions/pulse (0.5 %) and 250 kHz, respectively. Again, APEC was enabled using the Si^{2+}/Si^{+} as the tracking ratio. The field was then increased incrementally from a CSR(Si) of 0.25 to 200 (Fig. 10) and ~2 million ions collected at each condition. A voltage-based reconstruction was used for the PSM dataset [59], with spatial distributions maps applied for depth calibration using known interplanar spacings [64].

The evolution of the apparent Si isotope abundances during the PSM experiment are shown in Fig. 11(a) and in Fig. 11(b) for both charge-states. With an increase in electric field strength, significant deviations from the natural abundance are observed. More precisely, the fraction of ^{28}Si appears to decrease while the fractions of ^{29}Si and ^{30}Si increase. This may be expected since ^{28}Si, being the most abundant isotope, will have a

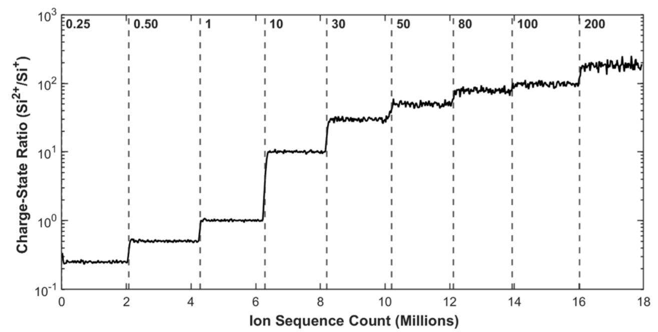

Fig. 10. CSR(Si) evolution as a function of ion sequence count for the APT analysis of the PSM.

higher probability of being involved in SISCS co-evaporation events, and leading to a larger detection loss [9]. The discrepancy in deviation between the singly- and doubly-charged Si states is most likely a combined effect of a higher background level at extremely high electric fields and reduced counting statistics due to a notably smaller number of total Si^{+} ions collected (e.g., ~0.5 % of the 2 million ions collected at a CSR(Si) of 200). As Si^{2+} is the dominant charge-state at high electric fields, where significant detection losses are thought to take place, it is used for all subsequent data analysis and correction schemes.

Based on this deviation, a double-hits correction factor (Fig. 12(a)) can be derived at each operating CSR(Si) following the procedure developed by Miyamoto et al. [35]. The corrected B dose, $B_{corrected}$, can then be given by,

$$B_{corrected} = \frac{B_{measured}}{B_{measured} + \frac{1-B_{measured}}{1-C\alpha}} \tag{2}$$

where $B_{measured}$ is the measured B dose, C is the square-sum of the Si isotope fractions ($\sum {X_{i_{Si}}}^2 \approx 0.853$), and α is a Si detection loss parameter. α is given by,

$$\alpha = \frac{C\left(\frac{n_{Si}}{X_{28_{Si}} n_{28_{Si}} + X_{29_{Si}} n_{29_{Si}} + X_{30_{Si}} n_{30_{Si}}}\right) - 1}{D\left(\frac{n_{Si}}{X_{28_{Si}} n_{28_{Si}} + X_{29_{Si}} n_{29_{Si}} + X_{30_{Si}} n_{30_{Si}}}\right) - C} \tag{3}$$

where n_{Si} is the total number of Si counts, $n_{28_{Si}}$, $n_{29_{Si}}$, and $n_{30_{Si}}$ are the total number of counts for each isotope, and D is the cube-sum of the Si isotope fractions ($\sum {X_{i_{Si}}}^3 \approx 0.784$). Fig. 12(b) shows the corrected B dose using Eq. (2) for the six samples as a function of the CSR(Si). In all cases, the corrected dose is less than the apparent value. However, the magnitude of correction increases with higher electric fields due to the higher Si detection loss. For the case of overestimation at the highest electric field, the correction scheme reduces the estimated dose from 104.7 % to 101.8 % of the expected value, now within the error range reported by NIST. Therefore, while a higher electric field does result in a slight reduction of Si quantification accuracy, the substantial improvement in the B measurement accuracy suggests that routine analysis of this material system should be performed at high electric fields.

It should be noted that there are inherent differences between the evaporation behaviour of the amorphous B-doped NIST sample and the crystalline Sb-doped PSM, meaning that the multi-hits and the magnitude of Si losses may differ. This implies that the correction factors may be slightly different for the PSM compared to the NIST sample. There is also the possibility that the observed deviations are not the result of Si SISCS co-evaporation detection loss, but rather formation of Si hydrides (e.g., SiH^{+}) with increasing electric field intensity (although, typically, the formation of molecular ions is higher at lower electric fields making such a trend improbable). As some of these Si hydrides would have a peak overlap with Si (e.g., $^{28}SiH^{+}$ with $^{29}Si^{+}$), the abundances would deviate, but the overall Si quantification would remain relatively

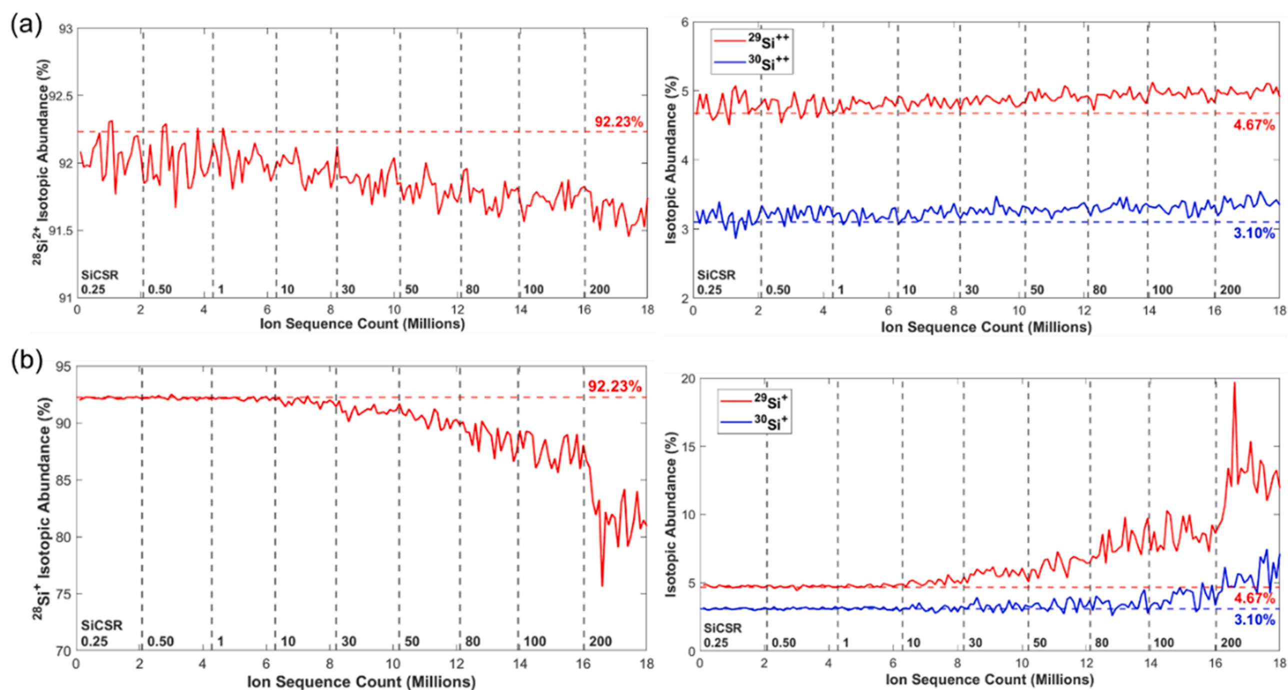

Fig. 11. Apparent Si isotope abundances evolution as a function of ion sequence count for (a) Si^{2+} and (b) Si^{+}.

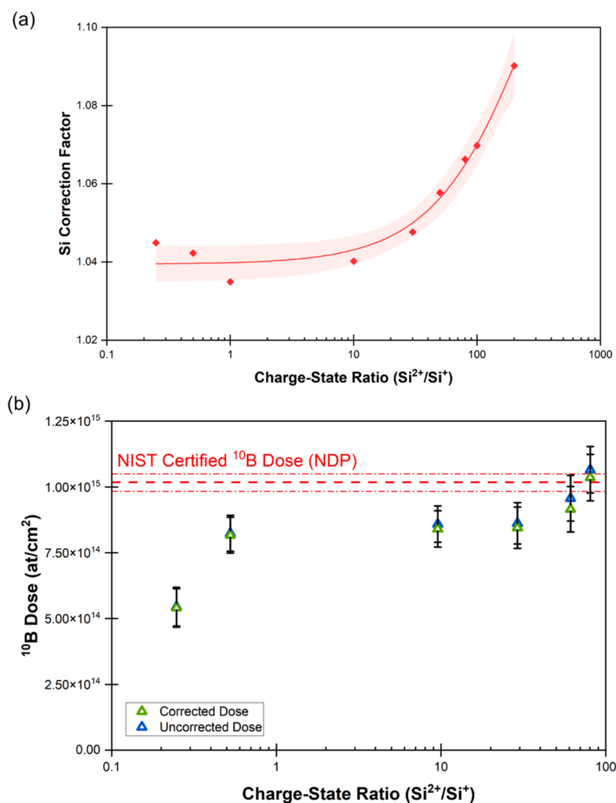

Fig. 12. (a) Si correction factor as a function of CSR(Si). (b) Corrected B doses using the Si double-hits correction factor for each sample.

accurate. However, the concentration of the Si hydride at 31 Da is relatively constant throughout the PSM experiment. As well, no peak was observed at 15.5 Da for SiH^{2+} and, in general, no hydrides are expected to form for the doubly-charged Si species [65]. Therefore, this assessment is still useful for providing a qualitative observation of the evaporation behaviour of Si as a function of electric field strength and illustrating its potential impact on the determined B dose.

4. Conclusion

B quantification accuracy using APT was investigated for a range of electric field conditions. A higher field was found to improve the B measurement accuracy in terms of dose and depth profile integrity. Reduced surface migration due to a highly homogeneous field on the specimen surface is proposed as the underlying mechanism behind this improvement. With less B mobility, there is a lower likelihood of B atoms coalescing and co-evaporating in SISCS multi-hit events, the dominant source of signal loss. The impact of the electric field strength on Si quantification was also investigated, whereby apparent isotope abundances suggest some detection losses at high fields. A correction scheme was presented, and B dose measurements were corrected to illustrate that observed Si losses account for only a small portion of the reported improvements. The results presented here offer a pathway for applying best practices in the application of APT for regular analysis of B-doped Si-based semiconductor devices.

CRediT authorship contribution statement

Bavley Guerguis: Writing – review & editing, Writing – original draft, Visualization, Investigation, Formal analysis, Conceptualization. **Ramya Cuduvally:** Writing – original draft, Investigation, Formal analysis, Conceptualization. **Richard J.H. Morris:** Writing – review & editing. **Gabriel Arcuri:** Writing – review & editing, Investigation. **Brian Langelier:** Writing – review & editing, Supervision, Project administration, Formal analysis. **Nabil Bassim:** Writing – review & editing, Supervision, Project administration, Funding acquisition.

Declaration of competing interest

The authors declare that they have no known competing financial interests or personal relationships that could have appeared to influence the work reported in this paper.

Data availability

Data will be made available on request.

Acknowledgements

The authors would like to thank the Natural Sciences and Engineering Research Council of Canada (NSERC) for supporting this work under the Discovery Grant program. All microscopy work presented here was carried out at the Canadian Center for Electron Microscopy (CCEM), a national facility supported by McMaster University, NSERC, and the Canada Foundation for Innovation (CFI). B.G. is grateful to Frederick Meisenkothen and Joe Bennett of the NIST for fruitful discussions.

References

[1] G. Orji, B. Bunday, Y. Obeng, International roadmap for devices and systems - metrology, in: 2022.

[2] S. Mirabella, D. De Salvador, E. Napolitani, E. Bruno, F. Priolo, Mechanisms of boron diffusion in silicon and germanium, J. Appl. Phys. 113 (2013), https://doi.org/10.1063/1.4763353.

[3] G. Schwarz, M. Trapp, R. Schimko, G. Butzke, K. Rogge, Concentration profiles of implanted boron ions in silicon from measurements with the ion microprobe, June 16. 17 (2021) 653–658. https://doi.org/10.1515/9783112499924-030.

[4] H. Takamizawa, Y. Shimizu, K. Inoue, T. Toyama, F. Yano, A. Nishida, T. Mogami, N. Okada, M. Kato, H. Uchida, K. Kitamoto, T. Miyagi, J. Kato, Y. Nagai, Correlation between threshold voltage and channel dopant concentration in negative-type metal-oxide-semiconductor field-effect transistors studied by atom probe tomography, Appl. Phys. Lett. 100 (2012), https://doi.org/10.1063/1.4730437.

[5] G. Mannino, S. Solmi, V. Privitera, M. Bersani, Electrical activation of B in the presence of boron-interstitials clusters, Appl. Phys. Lett. 79 (2001) 3764–3766, https://doi.org/10.1063/1.1423775.

[6] B. Gault, A. Chiaramonti, O. Cojocaru-Mirédin, P. Stender, R. Dubosq, C. Freysoldt, S.K. Makineni, T. Li, M. Moody, J.M. Cairney, Atom probe tomography, Nat. Rev. Methods Prim. 1 (2021), https://doi.org/10.1038/s43586-021-00047-w.

[7] T. Kinno, T. Sasaki, M. Tomita, T. Ohkubo, Quantitativeness in laser-assisted atom probe analysis of boron and carbon codoped in silicon, Jpn. J. Appl. Phys. 56 (2017), https://doi.org/10.7567/JJAP.56.116601.

[8] P. Dumas, S. Duguay, J. Borrel, F. Hilario, D. Blavette, Atom probe tomography quantification of carbon in silicon, Ultramicroscopy 220 (2021) 113153, https://doi.org/10.1016/j.ultramic.2020.113153.

[9] M. Thuvander, J.J. Weidow, J. Angseryd, L.K.L. Falk, F. Liu, M. Sonestedt, K. Stiller, H.O. Andrén, Quantitative atom probe analysis of carbides, Ultramicroscopy 111 (2011) 604–608, https://doi.org/10.1016/j.ultramic.2010.12.024.

[10] F. Meisenkothen, E.B. Steel, T.J. Prosa, K.T. Henry, R. Prakash Kolli, Effects of detector dead-time on quantitative analyses involving boron and multi-hit detection events in atom probe tomography, Ultramicroscopy 159 (2015) 101–111, https://doi.org/10.1016/j.ultramic.2015.07.009.

[11] A.J. Martin, B. Yatzor, Examining the effect of evaporation field on boron measurements in SiGe: insights into Improving the Relationship between APT and SIMS measurements of Boron, Microsc. Microanal. (2019), https://doi.org/10.1017/S1431927619000291.

[12] D. Melkonyan, Atomic scale observation of atom distributions in 3D devices using atom probe tomography, KU Leuven, 2019.

[13] T.E. Kelly, D.J. Larson, K. Thompson, R.L. Alvis, J.H. Bunton, J.D. Olson, B. R. Gorman, Atom probe tomography of electronic materials, Annu. Rev. Mater. Res. 37 (2007) 681–727, https://doi.org/10.1146/annurev.matsci.37.052506.084239.

[14] O. Cojocaru-Miŕdin, D. Mangelinck, D. Blavette, Nucleation of boron clusters in implanted silicon, J. Appl. Phys. 106 (2009), https://doi.org/10.1063/1.3265998.

[15] A.K. Kambham, J. Mody, M. Gilber, S. Koelling, W. Vandervorst, Atom-probe for FinFET dopant characterization, Ultramicroscopy 111 (2011) 535–539, https://doi.org/10.1016/j.ultramic.2011.01.017.

[16] O. Cojocaru-Mirédin, E. Cadel, F. Vurpillot, D. Mangelinck, D. Blavette, Three-dimensional atomic-scale imaging of boron clusters in implanted silicon, Scr. Mater. 60 (2009) 285–288, https://doi.org/10.1016/j.scriptamat.2008.10.008.

[17] W.K. Yeoh, S.W. Hung, S.C. Chen, Y.H. Lin, J.J. Lee, Quantification of dopant species using atom probe tomography for semiconductor application, Surf. Interface Anal. 52 (2020) 318–323, https://doi.org/10.1002/sia.6706.

[18] G.Da Costa, H. Wang, S. Duguay, A. Bostel, D. Blavette, B. Deconihout, Advance in multi-hit detection and quantization in atom probe tomography, Rev. Sci. Instrum. 83 (2012), https://doi.org/10.1063/1.4770120.

[19] M. Ngamo, S. Duguay, F. Cristiano, K. Daoud-Ketata, P. Pareige, Atomic scale study of boron interstitial clusters in ion-implanted silicon, J. Appl. Phys. 105 (2009), https://doi.org/10.1063/1.3126498.

[20] P. Ronsheim, P. Flaitz, M. Hatzistergos, C. Molella, K. Thompson, R. Alvis, Impurity measurements in silicon with D-SIMS and atom probe tomography, Appl. Surf. Sci. 255 (2008) 1547–1550, https://doi.org/10.1016/j.apsusc.2008.05.247.

[21] K. Thompson, J.H. Bunton, T.F. Kelly, D.J. Larson, Characterization of ultralow-energy implants and towards the analysis of three-dimensional dopant distributions using three-dimensional atom-probe tomography, J. Vac. Sci. Technol. B Microelectron. Nanom. Struct. 24 (2006) 421, https://doi.org/10.1116/1.2141621.

[22] D. Mangelinck, F. Panciera, K. Hoummada, M. El Kousseifi, C. Perrin, M. Descoins, A. Portavoce, Atom probe tomography for advanced metallization, Microelectron. Eng. 120 (2014) 19–33, https://doi.org/10.1016/j.mee.2013.12.018.

[23] Y. Tu, H. Takamizawa, B. Han, Y. Shimizu, K. Inoue, T. Toyama, F. Yano, A. Nishida, Y. Nagai, Influence of laser power on atom probe tomographic analysis of boron distribution in silicon, Ultramicroscopy 173 (2017) 58–63, https://doi.org/10.1016/j.ultramic.2016.11.023.

[24] S. Katnagallu, M. Dagan, S. Parviainen, A. Nematollahi, B. Grabowski, P.A.J. Bagot, N. Rolland, J. Neugebauer, D. Raabe, F. Vurpillot, M.P. Moody, B. Gault, Impact of local electrostatic field rearrangement on field ionization, J. Phys. D. Appl. Phys. 51 (2018), https://doi.org/10.1088/1361-6463/aaaba6.

[25] B. Gault, F. Danoix, K. Hoummada, D. Mangelinck, H. Leitner, Impact of directional walk on atom probe microanalysis, Ultramicroscopy 113 (2012) 182–191, https://doi.org/10.1016/j.ultramic.2011.06.005.

[26] S.C. Wang, T.T. Tsong, Field and temperature dependence of the directional walk of single adsorbed W atoms on the W(110) plane, Phys. Rev. B. 26 (1982) 6470–6475, https://doi.org/10.1103/PhysRevB.26.6470.

[27] J. Op De Beeck, Towards improved atom probe tomography analysis of semiconductors Unraveling the dynamic evolution of the semiconductor emitter, (2021).

[28] J.M. Hyde, M.G. Burke, B. Gault, D.W. Saxey, P. Styman, K.B. Wilford, T. J. Williams, Atom probe tomography of reactor pressure vessel steels: an analysis of data integrity, Ultramicroscopy 111 (2011) 676–682, https://doi.org/10.1016/j.ultramic.2010.12.033.

[29] D.R. Diercks, B.P. Gorman, R. Kirchhofer, N. Sanford, K. Bertness, M. Brubaker, Atom probe tomography evaporation behavior of C-axis GaN nanowires: crystallographic, stoichiometric, and detection efficiency aspects, J. Appl. Phys. 114 (2013), https://doi.org/10.1063/1.4830023.

[30] B. Gault, A. La Fontaine, M.P. Moody, A. Shariq, A. Cerezo, S.P. Ringer, G.D.W. Smith, Influence of surface migration on the spatial resolution of pulsed laser atom probe tomography, 044904 (2010). https://doi.org/10.1063/1.3462399.

[31] C. Oberdorfer, T. Withrow, L.J. Yu, K. Fisher, E.A. Marquis, W. Windl, Influence of surface relaxation on solute atoms positioning within atom probe tomography reconstructions, Mater. Charact. 146 (2018) 324–335, https://doi.org/10.1016/j.matchar.2018.05.014.

[32] Z. Peng, F. Vurpillot, P.P. Choi, Y. Li, D. Raabe, B. Gault, On the detection of multiple events in atom probe tomography, Ultramicroscopy 189 (2018) 54–60, https://doi.org/10.1016/j.ultramic.2018.03.018.

[33] F. Meisenkothen, M. Mclean, I. Kalish, D.V. Samarov, E.B. Steel, Atom probe mass spectrometry of uranium isotopic reference materials, Anal. Chem. 92 (2020) 11388–11395, https://doi.org/10.1021/acs.analchem.0c02273.

[34] R. Cuduvally, R.J.H. Morris, P. Ferrari, J. Bogdanowicz, C. Fleischmann, D. Melkonyan, W. Vandervorst, Potential sources of compositional inaccuracy in the atom probe tomography of In x Ga 1-x As, Ultramicroscopy 210 (2020) 112918, https://doi.org/10.1016/j.ultramic.2019.112918.

[35] G. Miyamoto, K. Shinbo, T. Furuhara, Quantitative measurement of carbon content in Fe-C binary alloys by atom probe tomography, Scr. Mater. 67 (2012) 999–1002, https://doi.org/10.1016/j.scriptamat.2012.09.007.

[36] L. Mancini, N. Amirifar, D. Shinde, I. Blum, M. Gilbert, A. Vella, F. Vurpillot, W. Lefebvre, R. Lardé, E. Talbot, P. Pareige, X. Portier, A. Ziani, C. Davesnne, C. Durand, J. Eymery, R. Butté, J.F. Carlin, N. Grandjean, L. Rigutti, Composition of wide bandgap semiconductor materials and nanostructures measured by atom probe tomography and its dependence on the surface electric field, J. Phys. Chem. C. 118 (2014) 24136–24151, https://doi.org/10.1021/jp5071264.

[37] D.S. Simons, R.G. Downing, G.P. Lamaze, R.M. Lindstrom, R.R. Greenberg, R. L. Paul, S.B. Schiller, W.F. Guthrie, Development of certified reference materials of ion-implanted dopants in silicon for calibration of secondary ion mass spectrometers, J. Vac. Sci. Technol. B Microelectron. Nanom. Struct. 25 (2007) 1365, https://doi.org/10.1116/1.2759937.

[38] K. Thompson, D.J. Larson, R.M. Ulfig, Pre-sharpened and flat-top microtip coupons: a quantitative comparison for atom-probe analysis studies, Microsc. Microanal. 11 (2005) 2004–2005, https://doi.org/10.1017/s1431927605502629.

[39] J.O. Douglas, P.A.J. Bagot, B.C. Johnson, D.N. Jamieson, M.P. Moody, Optimisation of sample preparation and analysis conditions for atom probe tomography characterisation of low concentration surface species, Semicond. Sci. Technol. 31 (2016), https://doi.org/10.1088/0268-1242/31/8/084004.

[40] K. Thompson, D. Lawrence, D.J. Larson, J.D. Olson, T.F. Kelly, B. Gorman, In situ site-specific specimen preparation for atom probe tomography, Ultramicroscopy 107 (2007) 131–139, https://doi.org/10.1016/j.ultramic.2006.06.008.

[41] D.R. Kingham, The post-ionization of field evaporated ions: a theoretical explanation of multiple charge states, Surf. Sci. 116 (1982) 273–301, https://doi.org/10.1016/0039-6028(82)90434-4.

[42] R. Cuduvally, B. Guerguis, B. Langelier, N.D. Bassim, C.M. Andrei, T. Casagrande, G.A. Arcuri, S. Russell, A correlative study of silicon carbide power devices using atom probe tomography and transmission electron microscopy, in: Conf. Proc. from Int. Symp. Test. Fail. Anal. 2023-Novem, 2023, pp. 500–508, https://doi.org/10.31339/asm.cp.istfa2023p0500.

[43] J. Bogdanowicz, A. Kumar, C. Fleischmann, M. Gilbert, J. Houard, A. Vella, W. Vandervorst, Laser-assisted atom probe tomography of semiconductors: the impact of the focused-ion beam specimen preparation, Ultramicroscopy 188 (2018) 19–23, https://doi.org/10.1016/j.ultramic.2018.03.001.

[44] C. Cappelli, A. Prez-Huerta, Testing the influence of laser pulse energy and rate in the atom probe tomography analysis of minerals, Microsc. Microanal. 29 (2023) 1137–1152, https://doi.org/10.1093/micmic/ozad057.
[45] C. Hatzoglou, S. Rouland, B. Radiguet, A. Etienne, G. Da Costa, X. Sauvage, P. Pareige, F. Vurpillot, Preferential evaporation in atom probe tomography: an analytical approach, Microsc. Microanal. 26 (2020) 689–698, https://doi.org/10.1017/S1431927620001749.
[46] R. Agrawal, R.A. Bernal, D. Isheim, H.D. Espinosa, Characterizing atomic composition and dopant distribution in wide band gap semiconductor nanowires using laser-assisted atom probe tomography, J. Phys. Chem. C. 115 (2011) 17688–17694, https://doi.org/10.1021/jp2047823.
[47] AP suite user guide, CAMECA instruments Inc. (2022).
[48] D. Larson, B. Geiser, T. Prosa, R. Ulfig, T. Kelly, Non-tangential continuity reconstruction in atom probe tomography data, Microsc. Microanal. 17 (2011) 740–741, https://doi.org/10.1017/s1431927611004570.
[49] T.J. Prosa, D. Olson, B. Geiser, D.J. Larson, K. Henry, E. Steel, Analysis of implanted silicon dopant profiles, Ultramicroscopy 132 (2013) 179–185, https://doi.org/10.1016/j.ultramic.2012.10.005.
[50] C.N. Singman, Atomic volume and allotropy of the elements, J. Chem. Educ. 61 (1984) 137–142, https://doi.org/10.1021/ed061p137.
[51] J.F. Ziegler, M.D. Ziegler, J.P. Biersack, SRIM - The stopping and range of ions in matter (2010), Nucl. Instru. Methods Phys. Res. Sect. B Beam Interact. Mater. Atoms. 268 (2010) 1818–1823, https://doi.org/10.1016/j.nimb.2010.02.091.
[52] W. Lefebvre-Ulrikson, F. Vurpillot, X. Sauvage, Atom probe tomography: put theory into practice, Academic Press, 2016.
[53] J. Bennett, Private communication, (2023).
[54] B. Gault, S.T. Loi, V.J. Araullo-Peters, L.T. Stephenson, M.P. Moody, S.L. Shrestha, R.K.W. Marceau, L. Yao, J.M. Cairney, S.P. Ringer, Dynamic reconstruction for atom probe tomography, Ultramicroscopy 111 (2011) 1619–1624, https://doi.org/10.1016/j.ultramic.2011.08.005.
[55] F. Meisenkothen, Private communication, in: 2023.
[56] F. Exertier, A. La Fontaine, C. Corcoran, S. Piazolo, E. Belousova, Z. Peng, B. Gault, D.W. Saxey, D. Fougerouse, S.M. Reddy, S. Pedrazzini, P.A.J. Bagot, M.P. Moody, B. Langelier, D.E. Moser, G.A. Botton, F. Vogel, G.B. Thompson, P.T. Blanchard, A. N. Chiaramonti, D.A. Reinhard, K.P. Rice, D.K. Schreiber, K. Kruska, J. Wang, J. M. Cairney, Atom probe tomography analysis of the reference zircon gj-1: an interlaboratory study, Chem. Geol. 495 (2018) 27–35, https://doi.org/10.1016/j.chemgeo.2018.07.031.
[57] D. Fougerouse, D.W. Saxey, W.D.A. Rickard, S.M. Reddy, R. Verberne, Standardizing spatial reconstruction parameters for the atom probe analysis of common minerals, Microsc. Microanal. 28 (2022) 1221–1230, https://doi.org/10.1017/S1431927621013714.
[58] S. Koelling, N. Innocenti, A. Schulze, M. Gilbert, A.K. Kambham, W. Vandervorst, In-situ observation of non-hemispherical tip shape formation during laser-assisted atom probe tomography, J. Appl. Phys. 109 (2011), https://doi.org/10.1063/1.3592339.
[59] B. Gault, M.P. Moody, J.M. Cairney, S.P. Ringer, Atom probe microscopy, Springer New York, New York, NY, 2012, https://doi.org/10.1007/978-1-4614-3436-8.
[60] D. Haley, T. Petersen, G. Barton, S.P. Ringer, Influence of field evaporation on radial distribution functions in atom probe tomography, Philos. Mag. 89 (2009) 925–943, https://doi.org/10.1080/14786430902821610.
[61] M.K. Miller, C.T. Liu, J.A. Wright, W. Tang, K. Hildal, APT characterization of some iron-based bulk metallic glasses, Intermetallics 14 (2006) 1019–1026, https://doi.org/10.1016/j.intermet.2006.01.040.
[62] Y.T. Ling, S. Cools, J. Bogdanowicz, C. Fleischmann, J. De Beenhouwer, J. Sijbers, W. Vandervorst, A bottom-up volume reconstruction method for atom probe tomography, Microsc. Microanal. 28 (2022) 1102–1115, https://doi.org/10.1017/S1431927621012836.
[63] J.R. De Laeter, J.K. Böhlke, P. De Bièvre, H. Hidaka, H.S. Peiser, K.J.R. Rosman, P. D.P. Taylor, Atomic weights of the elements: review 2000 (IUPAC technical report), Pure Appl. Chem. 75 (2003) 683–800, https://doi.org/10.1351/pac200375060683.
[64] B.P. Geiser, T.F. Kelly, D.J. Larson, J. Schneir, J.P. Roberts, Spatial distribution maps for atom probe tomography, Microsc. Microanal. (2007) 437–447, https://doi.org/10.1017/S1431927607070948.
[65] T.J. Prosa, E. Oltman, Study of LEAP® 5000 deadtime and precision via silicon pre-sharpened-microtip™ standard specimens, Microsc. Microanal. 28 (2022) 1019–1037, https://doi.org/10.1017/S143192762101206X.